JOURNAL OF AIRCRAFT
Vol. 47, No. 1, January–February 2010

Novel, Bidirectional, Variable-Camber Airfoil via Macro-Fiber Composite Actuators

Onur Bilgen,* Kevin B. Kochersberger,† and Daniel J. Inman‡
Virginia Polytechnic Institute and State University, Blacksburg, Virginia 24061
and
Osgar J. Ohanian III§
AVID LLC, Blacksburg, Virginia 24060

DOI: 10.2514/1.45452

This study aims to enable solid-state aerodynamic force generation in high-dynamic-pressure airflow. A novel, high-load-output, bidirectional variable-camber airfoil employing a type of piezoceramic composite actuator known as a Macro-Fiber Composite is presented. The novel airfoil employs two active surfaces and a single four-bar (box) mechanism as the internal structure. The unique choice of boundary conditions allows variable and smooth deformation in both directions from a flat camber line. The paper focuses on actuation modeling and response characterization under aerodynamic loads. A parametric study of aerodynamic response is employed to optimize the kinematic parameters of the airfoil. The concept is fabricated by implementing eight Macro-Fiber Composite 8557-P1-type actuators in a bimorph configuration to construct the active surfaces. The box mechanism generates deflection and camber change as predicted. Wind-tunnel experiments are conducted on a 12.6% maximum thickness, 127 mm chord airfoil. Aerodynamic and structural performance results are presented for a flow rate of 15 m/s and a Reynolds number of 127,000. Nonlinear effects due to aerodynamic and piezoceramic hysteresis are identified and discussed. A lift coefficient change of 1.54 is observed purely due to voltage actuation. Results are compared with conventional, zero-camber NACA and other airfoils. A 72% increase in the lift-curve slope is achieved when compared with a NACA 0009 airfoil.

I. Introduction

PIEZOCERAMICS remain the most widely used "smart" or active material because they offer high actuation authority and sensing over a wide range of frequencies. Specifically, piezoceramic materials have been extensively studied and employed in aerospace structures by performing shape and flow control. A Macro-Fiber Composite (MFC) is a type of piezoceramic device that offers structural flexibility and high actuation authority. A common disadvantage with piezoceramic actuators is that they require high-voltage input. In contrast, the current drain is extremely low, which creates small power consumption and requires relatively lightweight electronic components. With the continuing development of the electronic systems, active materials became feasible in small platforms such as unmanned air vehicles (UAVs) or micro air vehicles (MAVs). The purpose of this research is to exploit MFC actuation to perform shape control of an airfoil on small platforms and to determine the feasibility and advantages of smooth control surface deformations.

Smooth control surface designs have been a research interest since the beginning of modern aviation, with the first controlled, powered, and heavier-than-air flight by the Wright Brothers in 1903. During the past few decades, smart materials have been implemented to control the shape of continuous aerodynamic surfaces. Smart materials have also been used in flow control by adding energy to the flow by means of synthetic jets. Therefore, the following section lists the developments in the past few decades in aerodynamic applications via smart-material systems.

II. Developments in Aerodynamic Applications: Smart-Material-Based Systems

A. Morphing in Rotorcraft Applications

Lazarus et al. [1] examined the feasibility of using representative box wing adaptive structures for static aeroelastic control. It was found that greater control authority along with a lower weight penalty is achievable using adaptive aeroelastic structures for a variety of wing designs. Roglin et al. [2] presented an adaptive airfoil that uses a shape memory alloy actuator mechanism to actively change the camber of an airfoil for a remotely piloted helicopter. Steadman et al. [3] showed an application of a piezoceramic actuator for camber control in helicopter blades. Structure-control interaction was employed to develop an adaptive airfoil that could be used in the cyclic and vibration control of the helicopter. Giurgiutiu et al. [4] researched improvement on rotor blades using several smart-material-based technologies. A comprehensive review paper was published in 2000. In this paper, Giurgiutiu [5] reviewed achievements in the application of smart-materials actuation to counteract aeroelastic and vibration effects in helicopters and fixed-wing aircraft. Experiments of active flutter control, buffet suppression, gust load alleviation, and sonic fatigue reduction are discussed.

B. Morphing in Fixed-Wing Platforms

Conventional or smart-material-actuated continuous control surface designs have also been employed in fixed-wing aircraft. Jha and Kudva [6] studied how increasing or decreasing a wing

Presented as Paper 2133 at the 50th AIAA/ASME/ASCE/AHS/ASC Structures, Structural Dynamics, and Materials Conference 17th AIAA/ASME/AHS Adaptive Structures Conference, Palm Springs, CA, 4–7 May 2009; received 14 May 2009; revision received 11 August 2009; accepted for publication 11 August 2009.

*Ph.D. Candidate and Research Assistant, Department of Mechanical Engineering, Center for Intelligent Material Systems and Structures, 310 Durham Hall. Member AIAA.

†Research Associate Professor, Department of Mechanical Engineering, 201 Randolph Hall. Associate Fellow AIAA.

‡George R. Goodson Professor, Department of Mechanical Engineering, Center for Intelligent Material Systems and Structures, 315 Durham Hall. Fellow AIAA.

§Aircraft Design Engineer, 1750 Kraft Drive, Suite 1400; also Ph.D. Candidate, Department of Mechanical Engineering, Virginia Polytechnic Institute and State University, Blacksburg, Virginia 24061. Member AIAA.

parameter affects the performance of an aircraft, demonstrating that an optimal design requires large geometric changes to satisfy a multirole mission. Smooth cambering was applied in a Northrop Grumman Corporation unmanned combat air vehicle (UCAV) test model [7]. The unmanned aircraft demonstrated high actuation rate (80 deg/s), large deflection (20 deg), hingeless, smoothly contoured control surfaces with chordwise and spanwise shape variability. Piezoelectric motors were used as actuators. The camber control of wings using control surfaces has been extensively used in the industry as a morphing concept. Most of these designs use discrete and rotating leading- and trailing-edge controls. The F-16 Fighting Falcon uses leading-edge flaps to change the camber of the wings. In 2002, the Active Aeroelastic Wing program of NASA demonstrated twisting of wings for primarily roll control at trans- and supersonic speeds for an F/A-18 Hornet. The NASA Ames Research Center Mission Adaptive Wing Research program focused on producing smooth camber change by using a flexible internal mechanism to flex the outer skin. Drag was reduced by around 7% at the wing design cruise point and by 20% at an off-design condition. Moses et al. [8] used both an Active Fiber Composite (AFC, an earlier version of MFC) and MFC to actively reduce vibration levels in the tail fins of a wind-tunnel model of a fighter jet subjected to buffet loads. The fin-tip peak acceleration was reduced by about 70% with the MFCs and about 85% with the AFCs at frequencies near the first bending mode.

Along with the developments listed here, inflatable wings were mostly developed within the last few decades. Aspects of inflatable technologies and a review of inflatable wing and related technologies are included in Cadogan et al. [9,10]. More recent interest in inflatable wings was demonstrated through the development of an inflatable wing UAV for the U.S. Naval Research Laboratory by Vertigo, Inc. Flight tests of deployment and low-altitude flight of the design were conducted in 2001 by researchers at the NASA Dryden Flight Research Center [11]. The skeleton of the wing was made of inflatable tubes surrounded with crushable foam to provide the airfoil cross section. Simpson and Jacob [12] presented research on developing UAVs using inflatable wings with wing warping for roll control. The inflatable wings were constructed with internal bladders and flexible external restraints, and inflatable wing stiffness varied with internal pressure. A small-scale UAV with inflatable wings using wing warping roll control was demonstrated.

In recent years, several important advances have been centered on squeezing more performance out of existing adaptive materials and enhancing the performance of materials yet to come. The post-buckled precompression (PBP) concept in its earliest incarnation was primarily intended to increase the coupling coefficient exhibited by piezoelectric transducer elements [13]. Experiments showed that apparent coupling coefficients approaching one could be achieved by axially loading bending elements with forces that approached the buckling load of the beam. Vos et al. [14] conducted research to improve the PBP concept for aerodynamic applications. In this work, the design, modeling, and testing of a morphing wing for flight control of a UAV is presented. Axial precompression was generated in the piezoelectric elements by an elastic skin that covered the outside of the wing and served as the aerodynamic surface. It was shown that static trailing-edge deflections of ± 3.1 deg could be attained statically and dynamically through 34 Hz.

Seigler et al. [15] focused on modeling and flight control of large-scale planform altering flight vehicles. The equations of atmospheric flight were derived in a general form, methods of integrating the aerodynamic forces were examined, and various approaches and methods of flight control were distinguished.

C. Flow Control with Smart-Material Actuators

The use of conformal zero-mass flux actuators in aerodynamic flow control has been presented recently as a novel means of controlling the laminar separation bubble (LSB) on small aircraft subjected to low Reynolds number flows. Conformal zero-mass flux actuators include synthetic jets [16], plasma actuators [17], and piezoceramic actuators that move in the out-of-plane direction [18]. The motivation for designing such an actuator is to increase the bandwidth of actuation, for which the ability to delay or reattach the LSB is dependent on the excitation frequency and amplitude. Mechanical actuators are limited in frequency due to mass loading effects, whereas the MEMS actuators can operate at orders of magnitude higher frequency. There are also nonzero mass flux trailing-edge blowing (TEB) for circulation control, demonstrated in applications from helicopters [19] to turbine blades. The complexity and weight of TEB actuators make them a poor choice for small aircraft applications in which size, weight, and power are primary concerns. Acharya [20] presented the application of flow control technology to the compressor of a gas-turbine engine designed for a UCAV. Pulsed blowing was employed in the suction surface of stator vanes to delay or eliminate flow separation in the vane passage, thereby enabling higher vane loadings. Trailing-edge blowing was used in the inlet guide vanes to vector the flow leaving the vane row to desired flow angles.

Santhanakrishnan et al. [21] discussed several technologies for use on low-speed UAVs. These include adaptive wing technology that controls separation via active changes in the camber, the use of large-scale surface roughness to control separation, plasma actuators to control stall and enhance lift, and inflatable wings that can be tailored using wing warping. In the study, THUNDER piezoelectric actuators are employed in a cavity on the wing in which the actuator oscillation changes the profile of the suction surface. Gomes [22] investigated the effect of geometry and actuation variables on the peak jet velocity of a piezoelectric diaphragm synthetic jet actuator. Patel et al. [23] presented the use of dielectric barrier discharge plasma actuators for hingeless flow control over a 47 deg 1303 UCAV wing. When compared with the conventional trailing-edge devices, the plasma actuators demonstrated a significant improvement in the control authority in the 15–35 deg angle of attack range.

D. Morphing in Small Unmanned Aircraft

Continuous morphing concepts have also been used in smaller air vehicles. Researchers at the University of Florida have developed a series of MAVs that incorporate a unique, thin, reflexed, flexible wing design [24–27]. Garcia et al. [28] investigated the use of morphing as an effector to provide control authority. A torque tube actuated by servos twisted or curled the flexible wing. Flight tests show that wing twisting or curling was a good strategy to command roll maneuvers. Kim and Han [29] designed and fabricated a smart flapping wing by using a graphite/epoxy composite material and an MFC actuator. A 20% increase in lift was achieved in wind-tunnel tests by changing the camber of the wing at different stages of flapping motion.

Recently, Bilgen et al. [30,31] presented a new application for piezocomposite actuators on a 0.76-m-wingspan morphing wing air vehicle with approximately 0.815 kg of total weight. In this application, two MFC patches are bonded to the wings of a small demonstration vehicle, and the camber of the wing is changed with actuator voltage. This morphing control directly affects the circulation by changing the wing's camber, and adequate roll control authority is demonstrated in the wind tunnel as well as in flight. The aircraft demonstrates that lightweight, conformal actuators can be used as primary control surfaces on an aircraft. All electronics, including MFC power electronics (103 g), are powered by an 11.1 V lithium–polymer battery (106 g), a common choice for remotely controlled aircraft. The aircraft uses a 150 W brushless motor for thrust; in contrast, the MFC power electronics consume only 3.0 W during maximum morphing. Bilgen et al. recently presented static flow vectoring via an MFC-actuated bimorph airfoil [32] and a novel, MFC-actuated, bidirectional airfoil [33]. Wind-tunnel results and analytical evaluation of the airfoils showed comparable effectiveness to conventional actuation systems and no adverse deformation due to aerodynamic loading.

E. Current Research Motivation in Camber Control via Smart Materials

The motivation for the current research is to determine the aerodynamic effectiveness of a novel variable-camber control surface concept. The design is initially evaluated through wind-tunnel tests

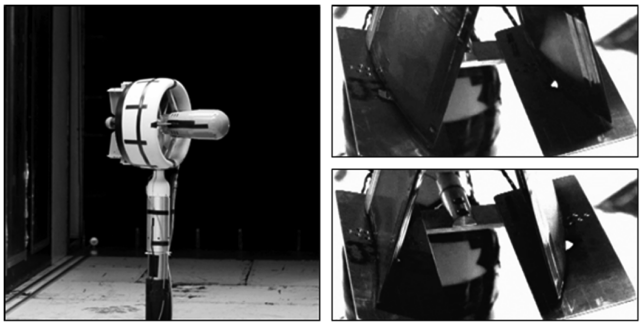

a) b)

Fig. 1 Wind-tunnel experiment: a) ducted fan vehicle model installed in the Virginia Polytechnic Institute and State University 6×6 ft^2 Stability Tunnel, and b) close-up of the two morphing control surfaces installed at the exit of the ducted fan.

of a vertical takeoff and landing (VTOL) MAV. The ducted fan, mounted on its side for wind-tunnel testing, and the two fabricated morphing airfoils, mounted at the exit of a ducted fan, are shown in Figs. 1a and 1b, respectively. The peak-to-peak displacement of the variable-camber airfoil (induced by voltage) is shown in Fig. 1b.

The wind-tunnel tests are conducted at a maximum fan flow speed of 45 m/s and a maximum freestream speed of 10 m/s. The morphing airfoil demonstrated high force outputs and no adverse deformation due to high aerodynamic loads. To prove the concept as a complete system, a custom, lightweight bipolar amplifier (weighing 151 g and capable of a ± 2 kV four-channel output) is fabricated and used during the wind-tunnel tests.

The VTOL application required a variable-camber airfoil design that can handle high dynamic pressure and symmetric deflection; however, the developments presented in this paper can easily be applied to a wide range of aerodynamic applications. Therefore, the current work focuses on fundamental (and isolated) airfoil characteristics, quantified in terms of conventional two-dimensional aerodynamic coefficients. First, the novel concept for variable-camber airfoil is introduced. The airfoil is theoretically evaluated for lift and drag performance at different configurations. Then a prototype airfoil is presented and wind-tunnel results are discussed. Finally, the paper concludes with a brief discussion of the results.

III. Macro-Fiber Composite Actuated, Variable-Camber Airfoil Concept

The high strain requirement under aerodynamic loads creates the need for semi-solid-state mechanisms to be employed along with piezoceramic actuation. A novel airfoil is designed to provide bidirectional aerodynamic vectoring. The design employs two active surfaces in the top and bottom surfaces of the airfoil, which are pinned at the trailing edge. These active surfaces are chosen to be MFC-actuated bimorph laminates. A compliant parallelogram (box structure) is used to create the desired boundary conditions at the front of the curved bimorph surfaces. Figure 2 shows the kinematic model and the parameters of the airfoil.

In the figure, β is the leading-edge (LE) incidence angle and MCL is the mean camber line. The compliant box can be simply described as a four-bar mechanism. The two parallel bars that connect the top and bottom surfaces have a constant length (L). The airfoil can be mounted to the vehicle either at the center or at the ends of the vertical bars. The change in camber of the active surface of the airfoil causes the box to comply and generate a shearlike motion while keeping the end-slope of the bimorphs equal to each other. When the airfoil is in nonactuated state, the link length (L) is equivalent to the LE thickness (T) of the airfoil. The initial percent thickness ($Th = L/\text{chord} \times 100$) is calculated at the 0 V state. It is important to note that the concept proposed here consists of 1) two active unimorph or bimorph surfaces, and 2) the three boundary conditions that are necessary to connect the surfaces and create a compliant mechanism. That is to say, the LE geometry is not

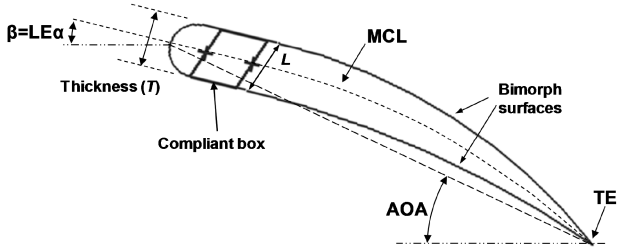

Fig. 2 Novel airfoil design and geometric parameters. The morphed state is illustrated.

proposed here, and it can be tailored to the specific application. In this study, the LE is designed to be elliptic due to geometric constraints of the VTOL shown in Fig. 1. Figure 3 shows a few possible geometric configurations with different link lengths and voltage inputs.

The airfoil thickness is determined depending on the application, in which an optimum configuration can be achieved for a desired function of various aerodynamic coefficients. The theoretical comparison of airfoils with different thicknesses is presented in the following section. Once the thickness is chosen, voltage could be applied to induce camber in both directions from a zero-camber state.

As mentioned earlier, an MFC-actuated bimorph is chosen as the active surface in the concept proposed here. The Macro-Fiber Composite actuator was developed at the NASA Langley Research Center [34,35]. An MFC is a layered, planar actuation device that employs rectangular cross-sectional, unidirectional piezoceramic fibers embedded in a thermosetting polymer matrix. The in-plane poling and subsequent voltage actuation allows the MFC to use the d_{33} piezoelectric effect, which is higher than the d_{31} effect used by traditional piezoelectric actuators with through-the-thickness poling [36]. There has been extensive analytical and experimental research focused on using MFC as an actuator (or sensor) for structural control. Williams [37] provides a detailed nonlinear characterization of the mechanical and piezoelectric behavior of the MFC actuator.

IV. Theoretical Aerodynamic Analysis

The theoretical analysis method presented here aims to determine the optimal thickness ratio of the airfoil for high lift authority. For the initial analysis, the airfoil is assumed to have a smooth and continuous surface and with a trailing-edge (TE) gap of 0.05% chord. A constant curvature is assumed for each surface of the active section due to the high chordwise coverage of the active material. An approximate slope of 2.86% camber per kilovolt is assumed for each active surface for the theoretical analysis. The linear assumption simply corresponds to 4.86% camber at 1700 V, 4.00% at 1400 V, and 2.00% at 700 V. A MATLAB®-based program is developed to drive the 2-D viscous panel method software XFOIL [38,39]. XFOIL software is employed to calculate the lift and drag coefficients and the pressure distribution. For XFOIL simulations, a 0.05% chord trailing-edge gap and an approximate 0.85% turbulence level is assumed. It must be noted that XFOIL predictions for an AOA above the maximum lift angle are not accurate. Because of the limitation of the deflection of the piezocomposite bimorph, the XFOIL analysis presented here never passes beyond this AOA limit.

Figure 4 shows the effective geometric parameters of the airfoils analyzed (illustrated in Fig. 3). All results presented in this section are for an LE incidence angle of 0 deg ($\beta = 0$). The AOA of the airfoil is decreased as the thickness is increased, which is caused by the change in location of the LE with respect to the TE. In contrast, the effective camber of the novel airfoil increases as the thickness is increased. This is because the mean camber line (the line that is equally distant from the top and bottom surface) forms a higher displacement with the increased thickness.

Figure 5 shows the theoretical change in lift and drag for the airfoil with 127 mm chord. The airfoil is subjected to a 15 m/s freestream velocity. The 2% thick airfoil reaches the $CL_{\max} = 1.12$ at 1400 V. The 6% thick airfoil shows the highest lift trend, and the 12% thick

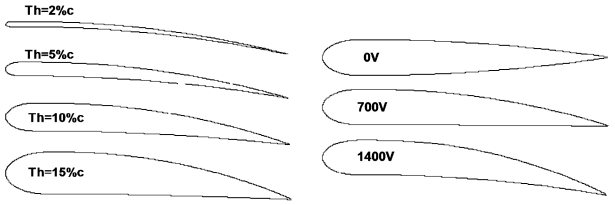

Fig. 3 Airfoil design: a) different vertical link lengths, and b) effect of voltage input ($Th = 13\%$).

airfoil shows the lowest drag trend. Considering the stiffness of the airfoil, the flow-induced deformation is assumed negligible at 15 m/s. A smooth surface is assumed for the analysis, which will be the main reason for the deviation of lift curve from actual performance around $CL_{\max}$. As reported in the literature, XFOIL predicts slightly high lift coefficient and low drag coefficient when compared with experimental results; therefore, the predictions must be viewed as an upper boundary to actual performance.

Figure 6 shows a comparison of lift over drag with actuation voltage. The maximum theoretical L/D is 42.6 for the 10% thick airfoil at 1300 V. This operation point corresponds to a camber of 4.12% and an AOA of 7.21 deg. The 2% thin airfoil shows the lowest L/D trend due to early stall and LE separation.

V. Displacement of the Airfoil with Custom DC–DC Converter

Using the conclusions derived from the analysis presented in Sec. IV and the geometric constraints of the VTOL aircraft described in Sec. II.E, two MFC-actuated airfoils are fabricated. A compliant box mechanism is designed to keep thickness to a minimum and allow free shear motion due to piezoceramic actuation. The elliptical leading edge is designed so that it could be mounted to the mounting bar directly or to the moving link (vertical link). In the latter case, the leading edge rotates with the vertical link in the opposite direction of the trailing edge. The gap between the leading edge and the rest of the airfoil is closed with a small flexible strip for smooth transition between the two surfaces. Figure 7 shows one of the two "identical" airfoils employing eight (four on each side) MFC 8557-P1-type actuators. The fabricated airfoil has a 15 mm thickness, a 127 mm chord, and a 133 mm span. The bimorphs are created by sandwiching a 25.4-μm-thick stainless steel sheet and bonding the laminate under vacuum. The substrate is chosen to be as thin as possible (to realize the optimum thickness ratio for a bimorph) and still have the desired spanwise rigidity. The MFCs are aligned at the TE in the chordwise direction.

A custom, lightweight bipolar amplifier, weighing 151 g and capable of a $+/-2$ kV four-channel output, is fabricated and used during the tests. Bench top static displacement tests are conducted to

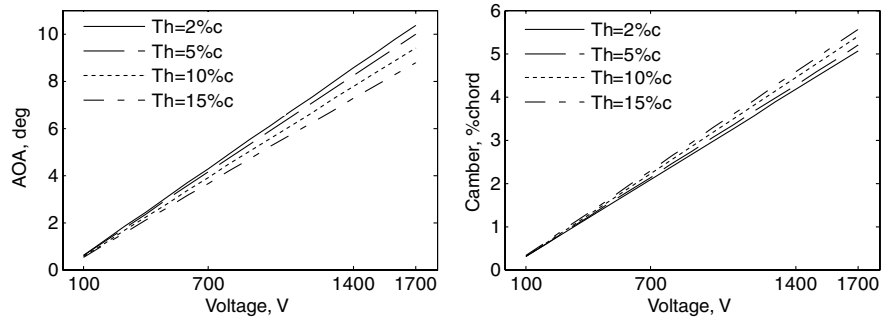

Fig. 4 Theoretical (2-D) change in geometry: a) angle of attack, and b) effective camber. Note that both the camber and AOA values are zero at 0 V due to linear assumption.

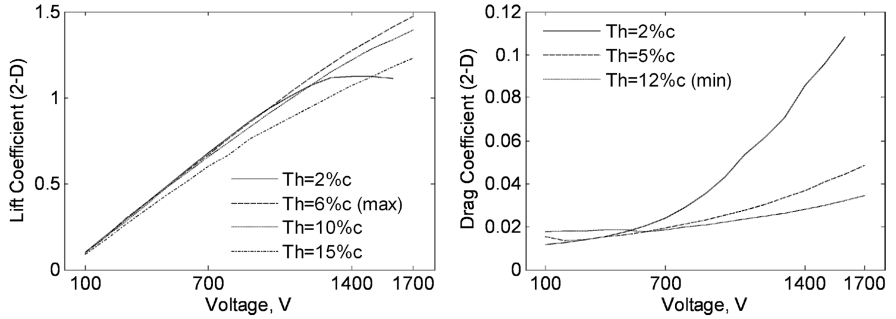

Fig. 5 Theoretical (2-D) results for the novel airfoil subjected to a freestream velocity of 15 m/s, $Re_{\text{chord}} = 1.27\text{E}5$: a) lift coefficient, and b) drag coefficient.

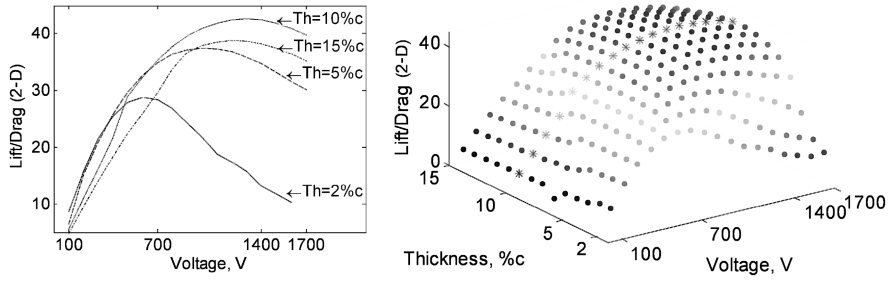

Fig. 6 Theoretical (2-D) L/D for the novel airfoil at 15 m/s, $Re_{\text{chord}} = 1.27\text{E}5$.

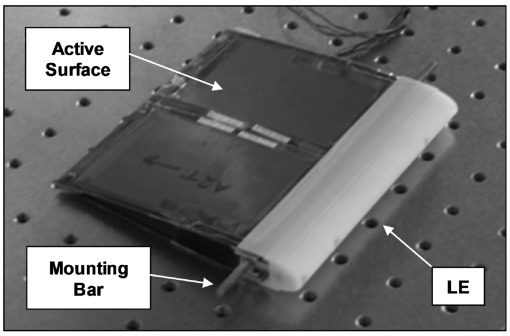

Fig. 7 Novel variable-camber airfoil with eight MFC 8557-P1 actuators; 127 mm chord and 133 mm span.

quantify the response of the airfoil as well as the custom amplifier. Note that the MFC actuators have a typical voltage range of −500 to 1500 V. Because the airfoil has two surfaces, both in a bimorph configuration, the MFCs on the opposite side are actuated with opposite voltage polarity and with a 3:1 fixed ratio. Figure 8 shows the experimental setup.

The amplifier is controlled (with a reference signal) using a National Instruments cDAQ data acquisition system. The amplifier has a 5 V source input supplied by an Agilent dc power supply. This power supply is used to measure the current draw by (and, hence, the power consumption of) the amplifier. High-voltage output to the MFCs is verified by two digital multimeters. The displacement of the airfoil is measured with a Micro-Epsilon optoNCDT 1401-200 laser displacement sensor. The displacement is measured at 86 mm from center of the compliant box (the mounting rod), which is equivalent to a distance of 118 mm from the leading edge. Figure 9 shows one of the airfoils at three different actuation levels.

Static voltage sweep tests are conducted to determine the nonlinearity of the amplifier voltage output and the airfoil displacement. First, a voltage level is set and steady-state displacement is achieved. The data are taken, and the next voltage level is applied. Figure 10 presents the voltage output of the amplifier, and the displacement of the airfoil is plotted against the user-input parameter labeled as the actuation percentage.

The plots represent a total of four loops (two loops for each airfoil) starting from −100 to +100 and back to −100%. The output of the amplifier is slightly nonlinear for both low- and high-side outputs. The amplifier output can be linearized by a simple analytic function if desired. The displacement shows hysteresis due to the piezoceramic nature of the MFC actuators. Note that each airfoil is tested twice, and both of these runs produce consistent displacement outputs. There is a small difference in the displacement output between the two airfoils for the positive actuation. This is expected considering the limited in-house fabrication methods. Both airfoils shows very high displacement outputs relative to other piezoceramic-actuated devices.

VI. Wind-Tunnel Setup and Flow Characterization

Wind-tunnel tests are performed in a low-speed, open-circuit wind tunnel located at the Center for Intelligent Material Systems and Structures (CIMSS). A custom mechanical beam balance is originally designed and then upgraded to incorporate two load cells (from Transducer Techniques) to measure lift and drag forces generated by the airfoil. A stepper-motor-driven rotary stage is used to set the angle of the airfoils tested. Figure 11 shows the wind-tunnel setup with the inlet nozzle located on the left of the picture and the downstream fans located on the right.

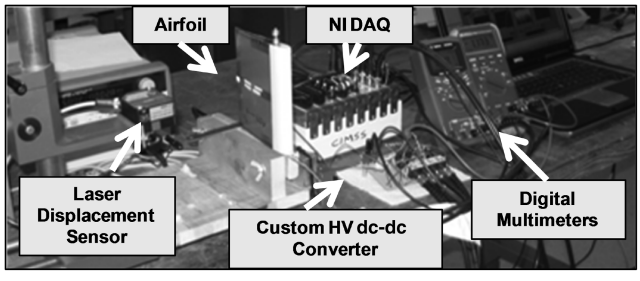

Fig. 8 Experimental setup for airfoil displacement measurements with bipolar amplifier.

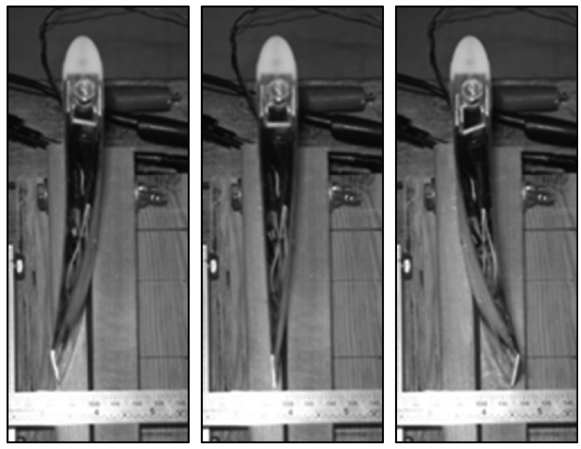

a) b) c)

Fig. 9 Displacement of the novel airfoil at three static voltage levels: a) −1500 V, b) 0 V, and c) +1500 V.

The leading edge of the test article is located at 58 cm from the beginning of the test section along the streamwise direction. The span axis is oriented normal to the floor of the test section (and ground.) The balance supports the test airfoil without contacting the tunnel walls. Figure 12 shows a simplified illustration of the test section and mechanical balance. As noted earlier, the mechanical balance used for the current tests employs two load cells; hence, the illustrations in Fig. 12 have some changes neglected that are not critical to the discussion. The airfoils tested in this study have an approximately 1.5 mm gap between the wing ends and the tunnel walls. Mueller and Burns [40] showed that gap sizes around 0.5% of the span are usually acceptable and do not affect the results. For the airfoils tested here, the gap is approximately 1.13%. Although the gap dimension is small, the percentage is still higher than recommended because of the low span of the airfoils. The possible effects of this gap size will be discussed in Sec. VI.B.

A. Velocity Profile and Turbulence Intensity

Preliminary tests are conducted to characterize the flow in the empty test section. Flow velocity during these tests is observed using a Flow-Kinetics pitot-static tube and a Setra 267 pressure transducer. Figure 13 shows the velocity profile along the horizontal ($y = 68$ mm) and vertical ($x = 178$ mm) axes. The temperature of the flow is measured using an Omega thermocouple and bridge amplifier and recorded for each run. The 20 s data sampled at 1 kHz is averaged to get the mean velocity. Although a 20 s sample is taken at each location, a variation of the mean value between each sample is still observed. This is known to be an effect of small and low-frequency disturbances in the lab and not because of the test-section geometry. Note that the wind tunnel used here is an open-circuit facility and a longer sample time would remove this mean velocity variation. For the horizontal axis velocity measurements, a mean velocity (solid line) of 15.4 m/s is measured and the 95% confidence interval uncertainty (dotted lines) is $U_{\text{Velocity},X} = +/-0.40$ m/s. For the vertical axis measurements, the mean velocity is 15.2 m/s and the 95% confidence interval uncertainty is $U_{\text{Velocity},Y} = +/-0.54$ m/s. An approximately 4% maximum difference from mean is calculated independent of pitot location. The flow is therefore assumed to be spatially uniform for coefficient calculations. The boundary layer will be discussed in the next section.

The streamwise turbulence of the flow in the empty test section is measured by a standard hot-wire anemometry technique. A TSI 1210-T1.5 probe is used along with a Dantec 55M01 bridge. The

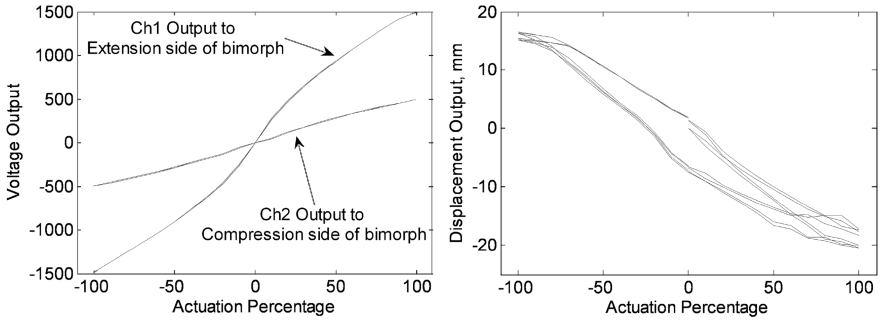

a) b)

Fig. 10 Benchmark experiments: a) amplifier voltage output, and b) airfoil displacement response to user input.

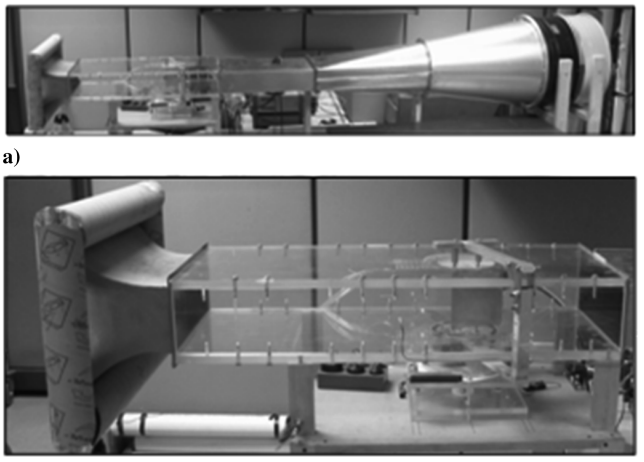

a)

b)

Fig. 11 Wind tunnel: a) complete setup, and b) close-up of the acrylic test section and inlet nozzle.

probe is located at the center of the test section for all turbulence tests. The signal is conditioned with a Frequency Devices model 9002 8-pole, 6-zero low-pass (LP) filter and an Ithaco 4302 dual 24 dB/octave high-pass (HP) filter. After proper conversion of the measured voltages to velocity (V), the turbulence intensity (TI) is calculated by

$$\mathrm{TI} = \frac{V_{\mathrm{rms}}}{V_{\mathrm{mean}}} \times 100, \quad \text{where } V_{\mathrm{rms}} = \sqrt{\frac{1}{n}\sum_{i=1}^{n}(V_i - V_{\mathrm{mean}})^2} \qquad (1)$$

where the index i represents each sample. Turbulence intensity is measured at several velocities for different filter settings. The presentation of turbulence for different bandwidths is commonly used in the literature [41] to show the frequency components of the turbulence. Note that the each measurement is repeated four times. Turbulence is calculated from each set and averaged to get a better representation of the mean turbulence intensity. Figure 14 presents turbulence intensity for different bandpass filter settings. The effect of the low-pass filter is small and not consistent at each velocity. This is caused by the reduction of power in the signal as frequency is increased, so that the roll-off of the filter is not completely effective. The variation of the turbulence observed in the figure is mostly due to the small change in turbulence with time and the change in mean velocity. The turbulence is at its lowest intensity around 15 m/s and highest at a 2 m/s average velocity. In contrast, the effect of the high-pass filter is significant, and as expected, the turbulence appears to decrease as more of the low-frequency content of the signal is filtered. Similarly, the lowest turbulence is observed at 15 m/s and the highest at 2 m/s. In summary, 0.60% turbulence intensity is calculated from 0.1 to 50 kHz bandpass filtered signal for the current test speed of 15 m/s. The turbulence of the wind tunnel used in this study is relatively larger than tunnels used in the research area due to the lack of flow straighteners/screens upstream of the inlet nozzle.

B. Baseline Aerodynamic Experiments on NACA Airfoils

A rapid-prototyped NACA 0009 airfoil is selected to compare the response of the CIMSS wind tunnel and mechanical balance with other facilities. The airfoil is tested for lift and drag coefficients at an average flow speed of 15 m/s and a chord Reynolds number of 127,000. The NACA 0009 airfoil has a maximum thickness of 11.3 mm, a span of $b = 133$ mm, and a chord of $c = 127$ mm. Tunnel wall effects and buoyancy corrections were applied as necessary using the techniques found in Barlow et al. [42]. The reported lift and drag coefficients are calculated by

$$C_l = C_{lu}(1 - \sigma - 2\epsilon_{\mathrm{sb}} - 2\epsilon_{\mathrm{wb}}) \qquad (2)$$

$$C_d = C_{du}(1 - 3\epsilon_{\mathrm{sb}} - 2\epsilon_{\mathrm{wb}}) \qquad (3)$$

Barlow suggests several corrections due to the existence of the walls around the airfoil. The solid blockage term, ϵ_{sb}, and the wake blockage terms are explained in Allen and Vincenti [43] and Maskell [44], respectively. C_{lu} and C_{du}, the uncorrected lift and drag coefficients, are calculated by

$$C_{lu} = F_{\mathrm{lift}}/(0.5\rho c b_r v_{\mathrm{qc}}^2) \qquad (4)$$

$$C_{du} = (F_{\mathrm{drag}} - F_{bd})/(0.5\rho c b_r v_{\mathrm{qc}}^2) \qquad (5)$$

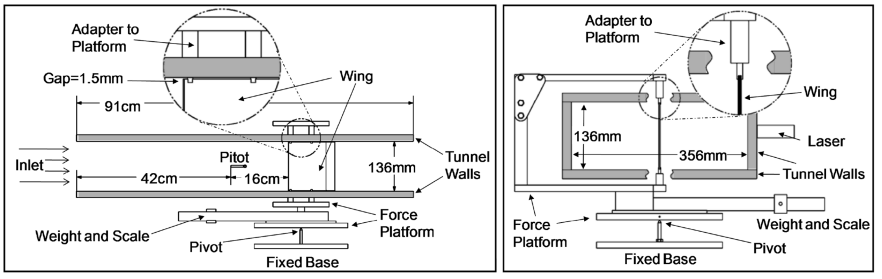

a) b)

Fig. 12 Wind-tunnel setup: a) side view with balance in drag configuration, and b) front view with balance in lift configuration.

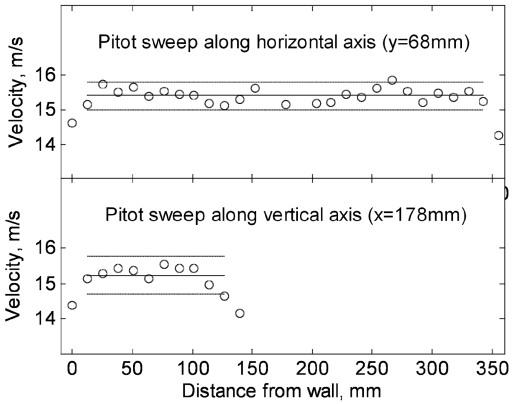

Fig. 13 Velocity profile of the empty test section measured 16 cm upstream of the airfoil.

where F_{lift} and F_{drag} are the measured lift and drag forces, and F_{bd} is the drag on the airfoil caused by the longitudinal pressure gradient. ρ is the density of air, b_r is the reduced span (due to boundary-layer displacement thickness), and v_{qc} is the flow speed calculated at the quarter-chord location. Note that density is calculated using the fixed absolute pressure in the lab and the temperature of the flow, which is recorded during each test. In addition, streamline curvature correction is applied, for which the angle of attack (α) is calculated by [43]

$$\alpha = \alpha_u + \frac{57.3}{2\pi}\left(\frac{\pi^2 c^2}{48h^2}\right)(C_{lu} + 4C_{m_{\frac{1}{4}}u}) \tag{6}$$

where α_u is the measured AOA, $h = 356$ mm is the section width, and $C_{m_{\frac{1}{4}}u}$ is the (negligible) uncorrected pitch-moment coefficient.

The actual velocity and reduction in span is calculated as follows. To begin, a calibration test is conducted in the empty test section between static ports (sufficiently upstream of the airfoil location) and the pitot-static tube located at different locations along the flow axis. The velocity is measured with the pitot-static tube at each location, and the development of the boundary layer (BL) is calculated by applying Bernoulli's equation and conservation of mass. The actual BL displacement thickness (from the calibration experiment) is approximately 5.0 mm. Because there is a 1.50 mm gap between the tunnel wall and the airfoil, the applied reduction in span is 6.62% of the actual span (b). The flow velocity during airfoil tests is calculated by applying the aforementioned calibration to the static-port measurement. Using the $1/7$ power velocity profile (assuming that flow is tripped at the inlet nozzle and, therefore, turbulent), the theoretical BL height is calculated to be 16.27 mm and the displacement thickness is 5.90 mm at a Reynolds number of 5.79E5 at the quarter-chord location [45].

Figure 15 presents a comparison of the NACA 0009 lift and drag coefficient data from the CIMSS wind tunnel with different tests done by Selig et al. at the University of Illinois [46,47]. The references and respective Reynolds numbers are presented in the legend of the figures. The measurements are recorded at a rate of 100 Hz for a period of 60 s to get an accurate mean. The data for the AOA sweep-up and sweep-down curves are presented for the current study; however, there was no measurable aerodynamic hysteresis observed. The tests are conducted at 15 m/s and a chord Reynolds number of 127,000.

The lift-curve slope matches relatively well considering the effect of turbulence. The Reynolds number has a negligible effect on the lift coefficient and there is no aerodynamic hysteresis. The drag coefficient from the current study shows a slightly higher trend at lower angles when compared with data reported by Selig et al. [46,47]. The 0 deg drag coefficient is 0.0158 for the NACA 0009 airfoil tested here. Selig et al. reported approximately 0.0087 at $Re = 150,000$ and 0.0096 at $Re = 100,000$ for the 0 deg drag coefficient of the NACA 0009 airfoil.

There are three main reasons for the difference in measured lift and drag between the two facilities compared in this section:

1) The span of the airfoils are designed so that the root and tip is as close to the wind-tunnel walls as possible. At high AOA, a small amount of 3-D flow exists through the 1.5 mm gap between the airfoil and the test-section walls.

2) The relatively large difference in turbulence levels in the two facilities must be noted. Selig et al. [46,47] report 0.358% rms turbulence for the 0.01 Hz cutoff frequency and 0.064% rms turbulence for the 1 Hz cutoff frequency at a Reynolds number of 100,000.

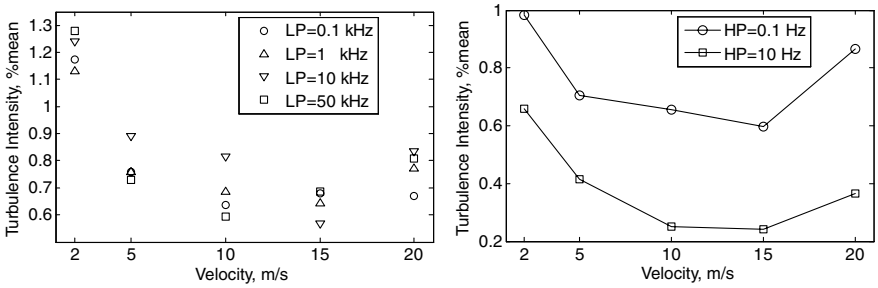

Fig. 14 Turbulence intensity vs velocity at the center of the empty test section: a) effect of LP filter with 0.1 Hz HP filter, and b) effect of HP filter with 50 kHz LP filter.

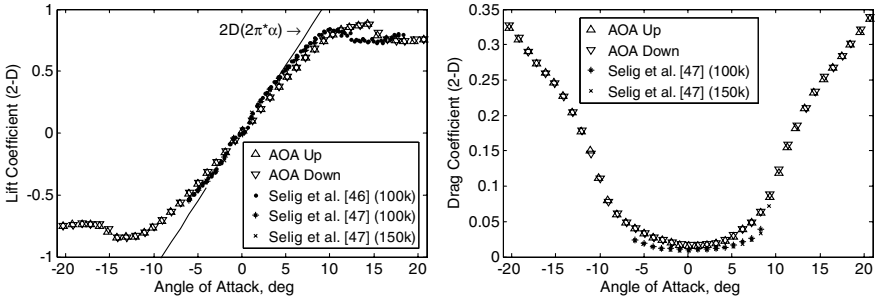

Fig. 15 Lift and drag coefficients vs angle of attack comparison for NACA 0009 airfoils.

3) Finally, the airfoil tested in this study is a rapid-prototyped airfoil with some roughness along the spanwise direction. It is known that the NACA 0009 airfoils used in [46,47] have a smoother surface.

The experimental measurements are prone to the relative errors induced by uncertainty in setting the mount angle, flexibility in the balance system, and a small amount of friction in the balance pivots. The absolute values have uncertainties due to several parameters, such as air density, flow velocity measurements, and the theoretical wall and BL corrections. The uncertainty analysis of each measurement is conducted by following the AIAA Standard [48]. The lift coefficient uncertainty is $U_{\mathrm{CL,max}} = \pm 0.055$ and the drag coefficient uncertainty is $U_{\mathrm{CD,max}} = \pm 0.014$. The major source for the uncertainty is the time variation of velocity.

VII. Aerodynamic Experiments on the Variable-Camber Airfoil

This section presents the aerodynamic experiments on the novel airfoil shown in Fig. 7. The measurement and calculation of lift, drag, and flow velocity is similar to the procedure outlined in the previous section. Because of the nature of the piezocomposite bimorph, the airfoil is expected to have a residual but predictable curvature due to hysteresis, even for a short-circuit condition. A nonlinear model is not addressed here; instead, the shape of the airfoil at each test condition is measured directly. This measurement is also necessary to observe the additional deformation (if any) due to aerodynamic loading.

A. Displacement Field Induced by Voltage Excitation

To obtain geometric parameters during the experiments, a fast and accurate method had to be employed using two laser displacement sensors and a digital camera. To begin, a calibration experiment is conducted for each airfoil. All geometric parameters are calculated from the image of the airfoil end section from the camera and correlated to the two laser displacement sensor measurements at the midspan section. The laser measurements are taken using two Micro-Epsilon laser displacement sensors with a 100 μm dynamic resolution mounted on the side wall of the acrylic test section. High spatial resolution can be obtained with the camera at the penalty of an increase in test time. The measurement is taken without airflow to limit aerodynamic effects. A direct correlation is obtained and the rest of the aerodynamic experiments are conducted with the laser sensors.

As noted earlier, the MFC actuators have a voltage range of approximately -500 to 1500 V. Because the airfoil has two surfaces, both in a bimorph configuration, MFCs on the opposite side are actuated with an opposite field and with a 3:1 fixed ratio. The higher of the two excitation voltages is used for labeling in the plots. A negative sign simply indicates actuation in the reverse direction. The standard definition of camber is used, in which the percent camber is the percentage of the height over the chord of the mean camber line. Figure 16 shows the displacement of the airfoil end section digitized from a series of six photos for a peak-to-peak voltage sweep.

The actuation voltage is swept from -1400 to 1400 and swept back to -1400 V. The effect of piezoelectric hysteresis can be observed from the difference between deflection at 0 V for the "up" and "down" sweeps. However, it should also be noted that the deflection is repeatable, as seen at the maximum positive and negative voltage levels. Figure 16 shows that the actual outline does deviate from the theoretical (and desired) airfoil. Most of this deviation occurs due to the interface between the active section and the rapid-prototyped LE.

B. Aerodynamic Response: Angle Sweep at a Fixed Voltage

The variable-camber airfoil is tested for its lift and drag performance at a flow speed of 15 m/s. Two different test schemes are followed. The first evaluation is performed by setting the voltage of the bimorph at a fixed value, then sweeping the support angle (β) up and down. The complete list of voltages (in order) is 1) -1500, 2) -700, 3) 0, 4) $+1500$, 5) $+700$, and 6) 0. The support angle is swept from -20 to 20 and back to -20 deg in 1 deg increments. Once the angle sweep is completed, the voltage is changed. The procedure outlined here is necessary for the correct identification and separation of two possible sources of nonlinear phenomena: 1) aerodynamic hysteresis, and 2) piezoceramic material hysteresis. These nonlinear effects will be discussed as the results are presented in the following paragraphs.

To identify deformation due to aerodynamic loading, baseline deflection measurements are taken with zero-flow velocity. The comparison of wind-on and wind-off conditions confirmed that there is no measurable deformation due to aerodynamic loading. All plots in Sec. VII represent the aerodynamically loaded data for consistency. Note that the angle of the support points (β) is given as the independent variable for the figures in this section, which is necessary for clear presentation of the data. The angle β is swept up and down for several voltage levels; however, aerodynamic hysteresis was not observed. The lack of aerodynamic hysteresis is expected due the turbulence level of the flow. The AOA and effective camber values derived from the laser displacement measurements are presented in Fig. 17. The measured change in AOA and camber is consistent with geometric predictions. The voltage-geometry relationship appears linear (and independent of β and magnitude of loading) because voltage is changed only when a β sweep is completed. It is observed that both the AOA and camber are nonzero values at 0 V. This is caused by the piezoceramic hysteresis (residual shape from a previous actuation test), which is a typical characteristic of an actuator that goes through high deformation. The hysteresis effect can be used to aid power consumption of the overall system, wherein the airfoil can carry a range of external loads without consuming any power (except the transient effort to reach the desired position.) As the support angle is swept up and down, no conclusive deformation is observed due to the change of aerodynamic load

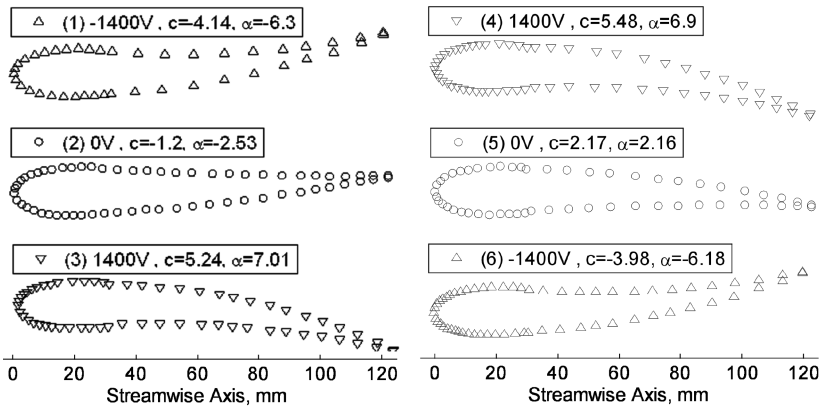

Fig. 16 Composite plot of the airfoil section measurements with digital camera. Legends show test order, voltage (V), camber (c), and the AOA (α) calculated.

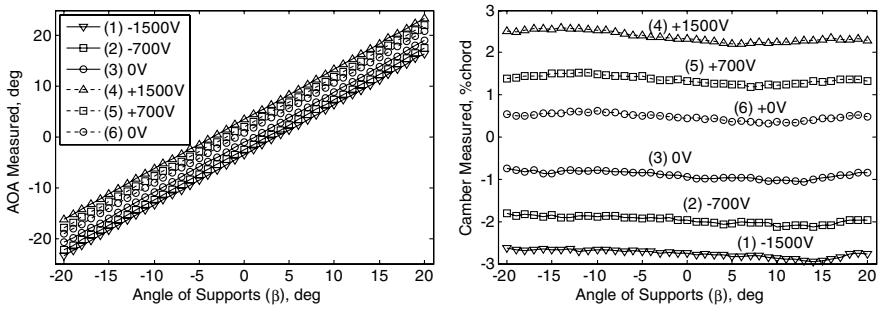

a) b)

Fig. 17 Structural response: a) angle of attack, and b) effective camber due to voltage input and the change in β. $Re_{\text{chord}} = 1.27\text{E}5$.

distribution on the airfoil. The airfoil sustains aerodynamic loading at 15 m/s.

Figure 18 presents the experimental results for the lift and drag coefficients versus the angle of support. The lift coefficient curves for the zero voltage levels have a slight offset due to the residual camber (and the induced angle), as noted earlier. The large voltage-induced peak-to-peak change in lift at 0 deg should be noted. Significant lift change is observed at a 0 deg support angle. A lift coefficient of -0.47 at -1500 V and 0.56 at 1500 V is observed, which results in a total lift change of 1.03 through voltage excitation at $\beta = 0$. The minimum drag observed is 0.032.

C. Aerodynamic Response: Voltage Sweep at a Fixed Support Angle

The first test scheme concluded that the aerodynamic hysteresis was negligible for the morphing airfoil tested. A second test scheme is designed to identify the hysteresis of the morphing airfoil due to its piezoceramic bimorph nature. The experimental setup and measurements are the same as the previous tests; however, only a fixed support angle of 0 deg is considered while the applied voltage is changed. The test is started at -1500 V. After force and displacement measurements are taken, the voltage is incremented by 100 V up to 1500 V, which is labeled as the sweep-up curve. The voltage is then swept down from 1500 to -1500 V in 100 V steps. As with the previous section, all plots represent the aerodynamically loaded airfoil.

Figure 19 presents the AOA and the camber of the airfoil. A 10.7 deg AOA change and 7.59% camber change is observed for the peak-to-peak actuation range. The nonlinear voltage-geometry relationship is due to piezoceramic hysteresis, which requires a feedback control if linearization is desired. The two measurement curves indicate that an increase in voltage magnitude above 1500 V will result in a slightly higher deflection. This is desired because the MFCs can safely be actuated up to 1700 V. Negative camber values simply indicate that actuation is in the negative direction.

Figure 20 shows the lift and drag coefficient versus the voltage input for the variable-camber airfoil at a 15 m/s flow speed. The lift coefficient is measured as -0.677 at -1500 V and 0.865 at $+1500$ V. The end slopes of the two curves indicate that higher lift can be achieved if voltage is increased. A change of 1.54 in the lift coefficient is calculated for the peak-to-peak voltage input. High drag is observed for the airfoil due to the relatively blunt LE and the discontinuities on the surface caused by the fabrication method. When drag and lift are evaluated together, a significant change in lift can be achieved for a small drag penalty. Such results confirm an important motivation for using a variable-camber airfoil without articulated surfaces.

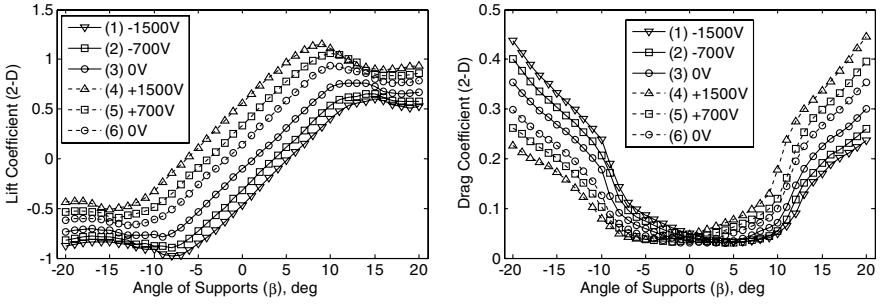

Fig. 18 Lift and drag coefficient (2-D) of the variable-camber airfoil at 15 m/s, $Re_{\text{chord}} = 1.27\text{E}5$.

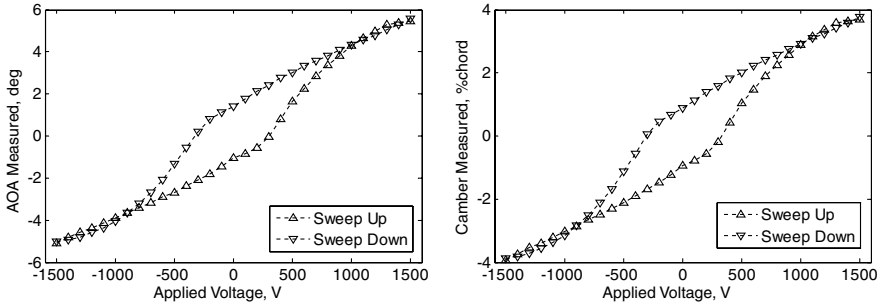

a) b)

Fig. 19 Structural response: a) AOA, and b) camber induced by voltage input at $\beta = 0$ deg. $Re_{\text{chord}} = 1.27\text{E}5$.

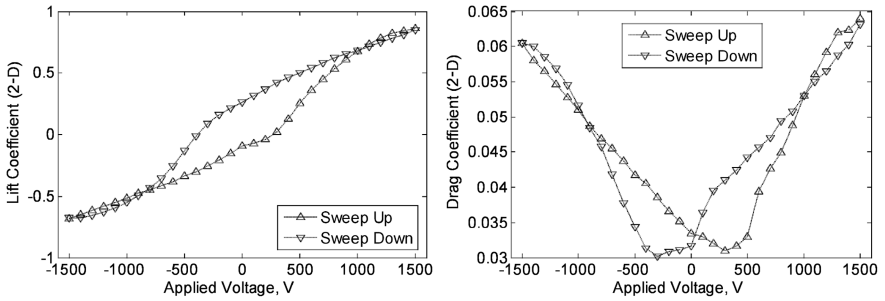

Fig. 20 Lift and drag coefficients (2-D) of the variable-camber airfoil at 15 m/s, $Re_{\text{chord}} = 1.27\text{E}5$.

D. Comparison of Variable-Camber Concept with Fixed-Camber Airfoils

An aerodynamic comparison of the variable-camber airfoil to other similar (in shape) fixed-camber airfoils is presented in this section. The authors aim to show the advantages of continuously coupled camber-AOA actuation when compared with the mechanical AOA actuation. Four airfoils are presented: 1) the novel variable-camber airfoil, 2) a NACA 0009 airfoil, 3) a NACA 0013 airfoil, and 4) a rapid-prototyped (RP) airfoil generated from the profile of the variable-camber prototype (at zero-camber state). The fourth airfoil is tested to determine the effects of the surface roughness. The NACA 0009 has a maximum thickness of 11.3 mm, and the NACA 0013 airfoil has a maximum thickness of 16.5 mm. The variable-camber and the RP airfoils have an equivalent thickness of 15 mm.

Figure 21 shows the profiles of the rapid-prototyped airfoils with a 133 mm span, a 127 mm chord, and a finite TE thickness of 1.0 mm. Lift and drag measurements are conducted at 15 m/s and at a chord Reynolds number of 127,000. The data are corrected for wall effects as outlined in the previous section. For the variable-camber airfoil, the true AOA (the voltage-induced AOA) is given as the independent variable. The mounting angle (β) is zero. In other words, there is no rotation of the airfoil supports for the morphing airfoil data presented. This allows a "fair" comparison between the fixed and variable-camber airfoils. Note that the AOA is calculated by photo calibration, as described earlier; hence, it introduces a negligible uncertainty to the original data given in Fig. 20.

The lift and drag comparison is given in Fig. 22. Note that the arrows in the legend specify the direction of sweep of voltage (volt) and AOA (α). There is a significant increase in lift due to camber induced by voltage input. A lift-curve slope of 0.144 per degree is measured, which exceeds the NACA 0009 lift slope (0.083 per degree) by 72%. The plot shows the clear advantage of the lift generation by a coupled camber-AOA change induced by voltage. The NACA 0013 and the RP airfoils develop similar lift-curve slopes; however, the NACA 0013 achieves a slightly higher $Cl_{\max}$. As noted earlier, high experimental drag is observed for the morphing airfoil due to its relatively blunt (elliptical) LE when compared with the LE of the NACA 0009 airfoil. The variable-camber prototype tested here does not have a continuous surface as desired due to in-house fabrication limitations. This is evident when the morphing airfoil at a 0 deg AOA is compared with its RP replica airfoil with a continuous and relatively smooth surface. Because the variable-camber airfoil is aimed at generating lift forces for vehicle control, the performance in lift is considered more important than the performance in drag.

The overall performance comparison of the airfoils is done by looking at the lift-over-drag (L/D) ratio presented in Fig. 23. The variable-camber airfoil produces a maximum L/D ratio of 13.4 at 1500 V ($\alpha = 5.78$ deg) and an L/D ratio of -11.2 at -1500 V ($\alpha = -5.20$ deg). The NACA 0009 airfoil produces a maximum L/D ratio of 16.3 at $\alpha = 4.21$ deg and an L/D ratio of -12.3 at $\alpha = -4.97$ deg. The variable-camber airfoil has higher L/D performance when compared with the fixed-camber airfoils with similar thicknesses (NACA 0013 and RP). In comparison with the

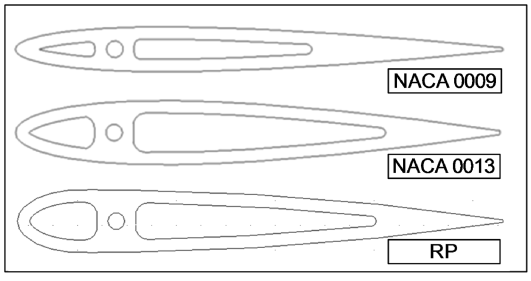

Fig. 21 Profiles of rapid-prototyped airfoils.

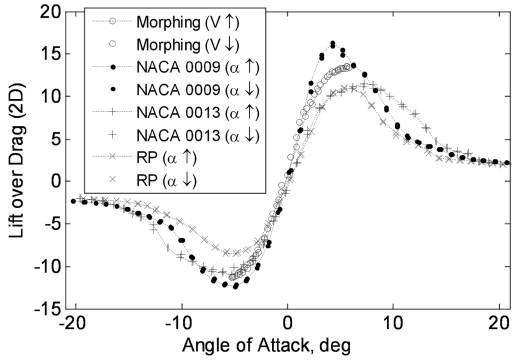

Fig. 23 Lift-over-drag (2-D) comparison at 15 m/s, $Re_{\text{chord}} = 1.27\text{E}5$.

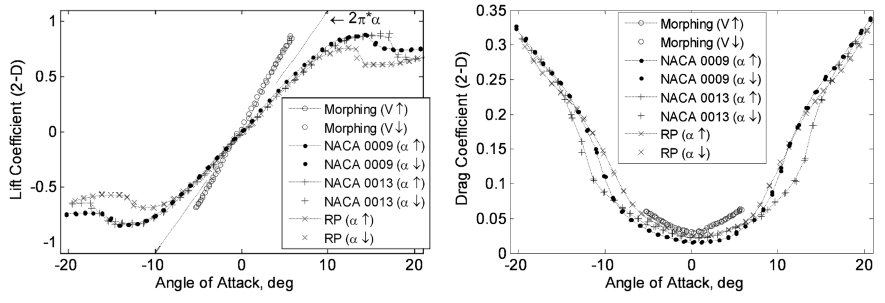

Fig. 22 Lift and drag coefficient (2-D) comparison at 15 m/s, $Re_{\text{chord}} = 1.27\text{E}5$.

conventional airfoils, the morphing airfoil generates a comparable change in lift over drag.

VIII. Conclusions

This paper presents research on novel actuators and power systems to demonstrate that smart materials can be employed for shape and flow control in UAVs or MAVs. There are several benefits of using camber control via solid-state active materials over trailing-edge control using conventional control surfaces in small air vehicles. First, the low Reynolds number flow regime can result in flow separation that reduces the effectiveness of a trailing-edge control surface. Second, power-limited aircraft such as small UAVs and MAVs cannot afford to lose energy through control surface drag. Finally, the opportunity for flow control is inherent in the active material due to its direct effect on circulation and its high operating bandwidth. In addition to replacing conventional control surfaces, these actuators can be effective in dynamic LSB control and any application in which flow vectoring is desired. The bandwidth advantage of a conformal actuator also opens the possibility for dynamic actuation that may have significant advantages.

For smart-material-actuated morphing devices, the challenge is found in operating a relatively compliant thin structure (desirable for piezoceramic actuators) at high dynamic pressures to extract controlling forces. Establishing a wing configuration that is stiff enough to prevent flutter and divergence but compliant enough to allow the range of available motion is the central challenge in developing a morphing wing. The concept presented here is designed to take advantage of aerodynamic loads to reduce control input moments and increase control effectiveness. The wind-tunnel results show comparable effectiveness to conventional actuation systems. MFCs demonstrate adequate control authority for aerodynamic shape control. The concept shows adequate stiffness at a tested flow speed of 15 m/s. An average lift coefficient increase of 1.54 is observed purely due to peak-to-peak actuation voltage. The concept showed a small increase in drag with actuation voltage, making it an efficient variable lift generation device. A maximum L/D ratio of 13.4 can be achieved through voltage excitation. Finally, a 72% increase in the lift-curve slope is achieved when compared with a NACA 0009 airfoil. Compared with previously published results, the concept presented in this research demonstrates high force outputs and frequency bandwidth (although not demonstrated in this paper). The concept is also tested and verified (in an unpublished AVID LLC test) to generate high control outputs in an experimental ducted fan vehicle.

Acknowledgments

This work is supported by the G. R. Goodson Professorship endowment, as well as the U.S. Air Force Research Laboratory through a Phase II Small Business Innovation Research contract with AVID LLC. The authors would like to thank colleagues at the Center for Intelligent Material Systems and Structures for their support.

References

[1] Lazarus, K. B., Crawley, E. F., and Bohlmann, J. D., "Static Aeroelastic Control Using Strain Actuated Adaptive Structures," *Journal of Intelligent Material Systems and Structures*, Vol. 2, July 1991, pp. 386–410.
doi:10.1177/1045389X9100200307

[2] Roglin, R. L., Hanagud, S. V., and Kondor, S., "Adaptive Airfoils for Helicopters," AIAA 1994-1764 , 1994.

[3] Steadman, D. L., Griffin, S. L., and Hanagud, S. V., " Structure-Control Interaction and the Design Of Piezoceramic Actuated Adaptive Airfoils," AIAA Paper 1994-1747, 1994.

[4] Giurgiutiu, V., Chaudhry, Z., and Rogers, C. A.,"Engineering Feasibility of Induced-Strain Actuators for Rotor Blade Active Vibration Control," *Smart Structures and Materials '94*, Vol. 2190, Society of Photo-Optical Instrumentation Engineers, Bellingham, WA, Feb. 1994, pp. 107–122; also Society of Photo-Optical Instrumentation Engineers Paper 2190-11.

[5] Giurgiutiu, V., "Review of Smart-Materials Actuation Solutions for Aeroelastic and Vibration Control," *Journal of Intelligent Material Systems and Structures*, Vol. 11, July 2000, pp. 525–544.
doi:10.1106/HYTV-NC7R-BCMM-W3CH

[6] Jha, A. K., and Kudva, J. N., "Morphing Aircraft Concepts, Classifications, and Challenges," *Proceedings of the Society of Photo-Optical Instrumentation*, Vol. 5388, Society of Photo-Optical Instrumentation Engineers, Bellingham, WA, 2004.
doi:10.1117/12.544212

[7] Bartley-Cho, J. D., Wang, D. P., and West, M. N., " Development, Control, and Test Results of High-Rate, Hingeless Trailing Edge Control Surface for the Smart Wing Phase 2 Wind Tunnel Model," *Smart Structures and Materials 2002: Industrial and Commercial Applications of Smart Structures Technologies*, Vol. 4698, Society of Photo-Optical Instrumentation Engineers, Bellingham, WA, 2002.
doi:10.1117/12.475100

[8] Moses, R. W., Weisman, C. D., Bent, A. A., and Pizzochero, A. E., "Evaluation of New Actuators in a Buffet Loads Environment," *SPIE 8th Annual International Symposium on Smart Structures and Materials*, Vol. 4332, Society of Photo-Optical Instrumentation Engineers, Bellingham, WA, 2001, pp. 10–21.

[9] Cadogan, D., Smith, T., Lee, R., Scarborough, S., and Graziosi, D., "Inflatable and Rigidizable Wing Components for Unmanned Aerial Vehicles," AIAA Paper 2003-6630, April 2003.

[10] Cadogan, D., Smith, T., Uhelsky, F., and Mackusick, M., "Morphing Inflatable Wing Development for Compact Package Unmanned Aerial Vehicles," AIAA Paper 2004-1807, April 2004.

[11] Murray, J., Pahle, J., Thornton, S., Frackowiak, T., Mello, J., and Norton, B., "Ground and Flight Evaluation of a Small-Scale Inflatable-Winged Aircraft," AIAA Paper 2002-0820, Jan. 2005.

[12] Simpson, A., and Jacob, J., "Aerodynamic Control of an Inflatable Wing Using Wing Warping," AIAA Paper 2005-5133, June 2005.

[13] Lesieutre, G., and Davis, C., "Can a Coupling Coefficient of a Piezoelectric Device be Higher Than Those of Its Active Material?," *Journal of Intelligent Material Systems and Structures*, Vol. 8, No. 10, 1997, pp. 859–867.
doi:10.1177/1045389X9700801005

[14] Vos, R., DeBreuker, R., Barrett, R., and Tiso, P., "Morphing Wing Fight Control Via Post-Buckled Precompressed Piezoelectric Actuators," *Journal of Aircraft*, Vol. 44, No. 4, July–Aug. 2007, pp. 1060–1069.
doi:10.2514/1.21292

[15] Seigler, T. M., Neal, D. A., Bae, J. S., and Inman, D. J., "Modeling and Flight Control of Large-Scale Morphing Aircraft," *Journal of Aircraft*, Vol. 44, No. 4, July–Aug. 2007, pp. 1077–1087.
doi:10.2514/1.21439

[16] Glezer, A., Amitay, M., and Honohan, A., "Aspects of Low- and High-Frequency Actuation for Aerodynamic Flow Control," *AIAA Journal*, Vol. 43, No. 7, 2005, pp. 1501–1511.
doi:10.2514/1.7411

[17] Pern, N. J., Jacob, J., and LeBeau, R., "Characterization of Zero Mass Flux Flow Control for Separation Control of an Adaptive Airfoil," AIAA Paper 2006-3032, June 2006.

[18] Ramakumar, K., and Jacob, J., "Flow Control and Lift Enhancement Using Plasma Actuators," AIAA Paper 2005-4635, June 2005.

[19] Rogers, E., Schwartz, A., and Abramson, J., "Applied Aerodynamics of Circulation Control Airfoils and Rotors," *Annual Forum Proceedings - American Helicopter Society*, Vol. 2, No. 41, 1985, pp. 479–490.

[20] Acharya, M., Emo, S., Bugajski, D., and Williams, D., "Smart Vanes for UCAV Engine Applications," AIAA Paper 2004-2516, July 2004.

[21] Santhanakrishnan, A., Pern, N. J., Ramakumar, K., Simpson, A., and Jacob, J. D., "Enabling Flow Control Technology for Low Speed UAVs," AIAA Paper 2005-6960, Sept. 2005.

[22] Gomes, L. D., Crowther, W. J., and Wood, N. J., "Towards A Practical Piezoceramic Diaphragm Based Synthetic Jet Actuator For High Subsonic Applications—Effect Of Chamber And Orifice Depth On Actuator Peak Velocity," AIAA Paper 2006-2859, June 2006.

[23] Patel, M. P., Ng, T. T., Vasudevan, S., Corke, T. C., and He, C., "Plasma Actuators for Hingeless Aerodynamic Control of an Unmanned Air Vehicle," *Journal of Aircraft*, Vol. 44, No. 4, July–Aug. 2007, pp. 1264–1274.
doi:10.2514/1.25368

[24] Ifju, P. G., Jenkins, D. A., Ettinger, S., Lian, Y., Shyy, W., and Waszak, M. R., "Flexible-Wing-Based Micro Air Vehicles," AIAA Paper 2002-0705, Jan. 2002.

[25] Waszak, M. R., Jenkins, L. N., and Ifju, P. G., "Stability and Control Properties of an Aeroelastic Fixed Wing Micro Aerial Vehicle," AIAA Paper 2001-4005, 2001.

[26] Albertani, R., Stanford, B., Hubner, J. P., Lind, R., and Ifju, P., "Experimental Analysis of Deformation for Flexible-Wing Micro Air

Vehicles," AIAA Paper 2005-2231 , May 2005.
[27] Torres, G. E., "Aerodynamics of Low Aspect Ratio Wings at Low Reynolds Numbers with Applications to Micro Air Vehicle Design," Ph.D. Dissertation, Aerospace and Mechanical Engineering Dept., Univ. of Notre Dame, Notre Dame, IN, April 2002.
[28] Garcia, H. M., Abdulrahim, M., and Lind, R., "Roll Control for a Micro Air Vehicle Using Active Wing Morphing," AIAA Paper 2003-5347, 2003.
[29] Kim, D. K., and Han, J. H., "Smart Flapping Wing Using Macro-Fiber Composite Actuators," *Proceedings of SPIE: The International Society for Optical Engineering*, Vol. 6173, 2006, pp. 133–141. doi:10.1117/12.658117
[30] Bilgen, O., Kochersberger, K., Diggs, E. C., Kurdila, A. J., and Inman, D. J., "Morphing Wing Micro-Air-Vehicles via Macro-Fiber-Composite Actuators," , AIAA Paper 2007-1785, April 2007.
[31] Bilgen, O., Kochersberger, K., Diggs, E. C., Kurdila, A. J., and Inman, D. J., "Morphing Wing Aerodynamic Control via Macro-Fiber-Composite Actuators in an Unmanned Aircraft," AIAA Paper 2007-2741, May 2007.
[32] Bilgen, O., Kochersberger, K., and Inman, D. J., "An Experimental and Analytical Study of a Flow Vectoring Airfoil via Macro-Fiber-Composite Actuators," *Proceedings of SPIE, Smart Structures/NDE*, Vol. 6930, Society of Photo-Optical Instrumentation Engineers, Bellingham, WA, March 2008. doi:10.1117/12.776448
[33] Bilgen, O., Kochersberger, K., and Inman, D. J., "A Novel Aerodynamic Vectoring Control Airfoil via Macro-Fiber-Composite Actuators," AIAA Paper 2008-1700, April 2008.
[34] Wilkie, W. K., Bryant, G. R., and High, J. W., "Low-Cost Piezocomposite Actuator for Structural Control Applications," *SPIE 7th Annual International Symposium on Smart Structures and Materials*, Society of Photo-Optical Instrumentation Engineers, Bellingham, WA, 2000, pp. 323–334. doi:10.1117/12.388175
[35] High, J. W., and Wilkie, W. K., "Method of Fabricating NASA-Standard Macro-Fiber Composite Piezoelectric Actuators," NASA TM-2003-212427, ARL-TR-2833, 2003.
[36] Hagood, N. W., Kindel, R., Ghandi, K., and Gaudenzi, P., "Improving Transverse Actuation Using Interdigitated Surface Electrodes," *North American Conference on Smart Structures and Materials*, Society of Photo-Optical Instrumentation Engineers, Bellingham, WA, 1993, pp. 341–352; also Society of Photo-Optical Instrumentation Engineers Paper 1917-25.
[37] Williams, R. B., "Nonlinear Mechanical and Actuation Characterization of Piezoceramic Fiber Composites," Ph.D. Dissertation, Dept. of Mechanical Engineering, Virginia Polytechnic Inst. and State Univ., Blacksburg, VA, March 2004.
[38] Drela, M., "XFOIL 6.9 User Primer, XFOIL: Subsonic Airfoil Development System," Massachusetts Inst. of Technology, Cambridge, MA, Nov. 2001, http://web.mit.edu/drela/Public/web/xfoil/xfoil_doc.txt.
[39] Drela, M., "XFOIL: An Analysis and Design System for Low Reynolds Number Airfoils," *Low Reynolds Number Aerodynamics*, edited by T. J. Mueller, Vol. 54, Lecture Notes in Engineering, Springer–Verlag, Berlin/New York/Heidelberg, June 1989.
[40] Mueller, T. J., and Burns, T. F., "Experimental Studies of the Eppler 61 Airfoil at Low Reynolds Numbers," AIAA Paper 82-0345, Jan. 1982.
[41] Selig, M. S., and McGranahan, B. D., "Wind Tunnel Aerodynamic Tests of Six Airfoils for Use on Small Wind Turbines," *Transactions of ASME, Series G: Journal of Dynamic Systems, Measurement and Control*, Vol. 126, Nov. 2004, pp. 986–1000. doi:10.1115/1.1793208
[42] Barlow, J. B., Rae, W. H. Jr., and Pope, A., *Low-Speed Wind Tunnel Testing*, 3rd ed., Wiley, New York, 1999.
[43] Allen, H. J., and Vincenti, W. G., "Wall Interference in a Two-Dimensional-Flow Wind Tunnel with Consideration of the Effect of the Compressibility," NACA TR 782, 1944.
[44] Maskell, E. C., "A Theory of the Blockage Effects on Bluff Bodies and Stalled Wings in a Closed Wind Tunnel," Aeronautical Research Council R&M 3400, 1965.
[45] Fox, R. W., McDonald, A. T., and Pritchard, P. J., *Introduction to Fluid Mechanics*, 6th ed., Wiley, New York, 2004.
[46] Selig, M. S., Guglielmo, J. J., Broeren, A. P., and Giguere, P., *Summary of Low-Speed Airfoil Data*, Vol. 1, Soartech Publications, Virginia Beach, VA, 1995.
[47] Selig, M. S., Donovan, J. F., and Fraser, D. B., *Airfoils at Low Speeds: Soartech 8*, H. A. Stokely, Virginia Beach, VA, 1989.
[48] "AIAA Standard on Assessment of Experimental Uncertainty with Application to Wind Tunnel Testing," AIAA, S-071A-1995, New York, 1995.